Vietnam Journal of Earth Sciences, 48(4), 487−512, https://doi.org/10.15625/2615-9783/24546

Vietnam Journal of Earth Sciences
https://vjs.ac.vn/index.php/jse

Deep learning-based mapping of land subsidence susceptibility using InSAR and geospatial data

Nguyen Thanh Tuan[1], Phan Trong Trinh[2], Khac Vu Dang[3], Dam Duc Nguyen[1], Tran Van Phong[2], Nguyen Duc Anh[2], Dao Ngoc Dung[4], Indra Prakash[5], Binh Thai Pham[1,*]

[1]*Geotechnical and Artificial Intelligence research group, University of Transport Technology, Hanoi, Vietnam*
[2]*Institute of Earth Sciences, VAST, Hanoi, Vietnam*
[3]*Ha Noi National University of Education, Hanoi, Vietnam*
[4]*Thai Binh University, Hung Yen, Vietnam*
[5]*DDG (R) Geological Survey of India, Gandhinagar 382010, India*

Received 14 March 2026; Received in revised form 20 April 2026; Accepted 23 April 2026

ABSTRACT

Land subsidence is one of the geotechnical phenomena that significantly affects infrastructure, construction, and sustainable urban development. Therefore, predicting and identifying areas susceptible to land subsidence has received increasing attention in recent studies. This study examines the application of deep learning models to spatial data analysis for predicting land subsidence susceptibility in the Hanoi area. Land subsidence data were obtained from satellite imagery and processed using a multi-temporal InSAR approach to determine surface deformation. They were then split into two datasets: 70% for training and 30% for validation. A total of 19 conditioning factors were used as input variables for the models, including aspect, slope, curvature, elevation, normalized difference vegetation index (NDVI), groundwater, engineering geology, hydrogeology, Holocene sediment thickness, land use/land cover (LULC), rainfall, topographic wetness index (TWI), and Landsat 8 spectral Bands 1–7. Four deep learning models, including CNN, LSTM, DRDN, and CNN-LSTM, were developed and compared to evaluate their predictive capability. The performance of the models was assessed using AUC, RMSE, MAE, and other evaluation metrics. The results show that all four models achieved good predictive performance, among which the DRDN model provided the best overall results, with AUC = 0.984, MAE = 0.064, and RMSE = 0.254 for the training dataset, while the corresponding values for the validation dataset were AUC = 0.957, MAE = 0.093, and RMSE = 0.305, indicating that the model has high accuracy and strong generalization capability in mapping land subsidence susceptibility in the study area. In addition, SHAP analysis revealed that Holocene sediment thickness and groundwater were the most important factors controlling land subsidence susceptibility in Hanoi.

Keywords: Artificial neural networks, InSAR, deep learning, GIS, land subsidence, Hanoi, Vietnam.

1. Introduction

Land subsidence, caused by both natural processes and human activities, is a widespread phenomenon worldwide (Galloway et al., 2011; Holzer et al., 2005). In urban areas, this phenomenon is often closely associated with excessive groundwater extraction, increased loading from construction activities, and changes in geological and hydrogeological conditions

*Corresponding author, Email: binhpt@utt.edu.vn

(Nozadkhalil et al., 2023; Younas et al., 2023), as well as the collapse of karst sinkholes (Liu Xingzong et al., 2024; Pan et al., 2022) or the oxidation of organic soil layers. Land subsidence can cause significant negative impacts on urban infrastructure, buildings, transportation systems, and socio-economic activities, particularly in areas with weak soil conditions or complex geological settings. Therefore, investigating the spatial and temporal characteristics of land subsidence is of great importance for identifying high-risk areas, supporting urban planning, and mitigating geological hazards.

Assessing the risks and damages from land subsidence is closely linked to monitoring ground deformation and surface movement. Currently, several techniques are used to investigate land subsidence, including geodetic surveying methods (Abidin et al., 2010; Abidin et al., 2001), extensometers (Wu et al., 2010), Global Navigation Satellite Systems (Ikehara et al., 1994; Teatini et al., 2005), and remote sensing techniques such as Differential Interferometric Synthetic Aperture Radar (DInSAR, PS-InSAR, SBAS, COSMO-SkyMed) (Hong, 2024; Lenardón Sánchez et al., 2024; Sun et al., 2023). Traditional monitoring methods require expensive equipment and provide deformation measurements only at discrete locations; therefore, they are mainly used for precise deformation measurements after subsidence events occur. In contrast, remote sensing techniques utilize two or more radar images acquired at different times over the same area to estimate surface deformation and ground displacement over large spatial scales.

Differential Interferometric Synthetic Aperture Radar (DInSAR) is a technique that measures ground displacement by analyzing the phase differences of radar signals acquired from two SAR images captured at different times over the same area (Massonnet et al., 1998). DInSAR offers several advantages for monitoring ground deformation; however, it also has certain limitations, including temporal decorrelation and phase disturbances caused by atmospheric effects (Massonnet et al., 1995; Zebker et al., 1992). Therefore, advanced techniques have been developed to improve the accuracy and reliability of InSAR-based deformation analysis. In recent years, several improved approaches have been proposed to enhance InSAR performance, particularly in reducing noise and increasing the accuracy of ground deformation measurements. One of the most widely used techniques is Persistent Scatterer Interferometric Synthetic Aperture Radar (PS-InSAR).

In recent years, remote sensing technology and Geographic Information Systems (GIS) have developed rapidly, significantly improving the efficiency and accuracy of land subsidence susceptibility mapping. The integration of GIS-based spatial analysis with remotely sensed data has enabled more reliable assessments of surface deformation and environmental conditions associated with subsidence. Numerous studies have investigated the spatial relationships between land subsidence and its controlling factors (Chai et al., 2024; Ku et al., 2023). Several researchers have also applied machine learning models combined with thematic maps to generate land subsidence susceptibility maps. These approaches include fuzzy logic models (Faryabi, 2023; Karimiasl et al., 2024), evidential belief functions (Eghbali et al., 2024), support vector machines (Li et al., 2023; Mehrnoor et al., 2023), logistic regression models (Hosseinzadeh et al., 2024; Sekkeravani et al., 2022), artificial neural networks (Yu et al., 2022), alternating decision trees (Zhao et al., 2024),… These models have shown promising performance in identifying subsidence-prone areas and analyzing the influence of environmental factors. However,

many expert-based or knowledge-driven models rely heavily on subjective judgments during model construction and parameter selection. Such dependence on expert interpretation may introduce bias and reduce the objectivity and reliability of the resulting land subsidence maps.

Deep learning is a branch of machine learning that builds on artificial neural networks (ANNs). It employs deep neural networks consisting of multiple hidden layers to learn complex representations from data (Tuan et al., 2024). These layers act as sequential filters that progressively extract features from simple patterns to more complex structures. Unlike traditional machine learning algorithms that require manual feature engineering, deep learning models can automatically learn hierarchical features directly from raw data such as images, audio signals, and text with minimal human intervention (Nguyen et al., 2024). Deep learning has demonstrated remarkable performance in both classification and regression tasks. It has been widely applied across various fields, including image recognition, natural language processing, machine translation, medical diagnosis, and financial analysis (Nguyen et al., 2025). Owing to their deep architectures and ability to process large datasets, deep learning models often achieve higher predictive accuracy compared to many traditional machine learning approaches. In the context of land subsidence research, several deep learning architectures have been applied to improve susceptibility mapping and deformation analysis. For example, Convolutional Neural Networks (CNN) have been used to extract spatial features from geospatial data (Liu Kai et al., 2024), while hybrid models combining CNN with Recurrent Neural Networks (RNN) have been proposed to capture both spatial and temporal characteristics of subsidence processes (Kariminejad et al., 2024). Overall, deep learning models generally provide better predictive capability than traditional machine learning techniques. However, despite their advantages in handling large and complex datasets, conventional machine learning methods remain useful in situations where datasets are limited or computational resources are constrained (Ahmed et al., 2023).

Therefore, selecting an appropriate modeling approach should depend on the problem's characteristics and the available data. In this study, a multi-temporal InSAR approach, Geographic Information Systems (GIS), and deep learning models were integrated to detect, monitor, and map land subsidence susceptibility. The main objectives of this study are: (1) to estimate surface deformation fields to identify and map subsidence-prone areas; (2) to develop land subsidence susceptibility maps using several deep learning models; and (3) to evaluate the influence of environmental conditioning factors on land subsidence and determine the optimal predictive model based on evaluation metrics such as prediction accuracy and the area Under the Receiver Operating Characteristic Curve (AUC).

2. Methodology

2.1. Convolutional Neural Network (CNN)

Convolutional Neural Networks (CNNs) are deep learning architectures that automatically learn spatial feature representations from input data via convolutional operations (Nguyen et al., 2026). Instead of relying solely on fully connected transformations, CNN employs learnable filters that slide across the input to capture local spatial patterns and feature correlations. These extracted features are then transformed through nonlinear activation functions, typically the Rectified Linear Unit (ReLU), which enhances the model's

capability to represent complex nonlinear relationships (Kumar et al., 2025).

Through hierarchical feature learning, CNN progressively converts raw input data into high-level representations that are more informative for prediction tasks. Model parameters are commonly optimized using gradient-based optimization algorithms such as Adam, which improves training efficiency and convergence stability (Dang et al., 2022). Owing to its strong ability to extract spatial features and model nonlinear relationships, CNN has been widely applied to classification problems involving structured or spatially correlated datasets.

2.2. Long Short-Term Memory (LSTM)

Long Short-Term Memory (LSTM) is an advanced recurrent neural network architecture designed to capture long-term dependencies in sequential data (Pham et al., 2026). Conventional recurrent neural networks often suffer from gradient instability during training, limiting their ability to retain information across long sequences. LSTM addresses this issue by introducing memory cells together with gating mechanisms that regulate the flow of information within the network. Within the LSTM structure, activation functions such as sigmoid and hyperbolic tangent (tanh) are employed to control information updates and memory retention. This mechanism enables the model to selectively preserve relevant information over multiple time steps while filtering out less important signals. As a result, LSTM can learn complex temporal relationships in sequential datasets (Nguyen et al., 2026). Due to its memory capability, LSTM has demonstrated strong effectiveness in classification tasks where sequential patterns or temporal dependencies exist in the data.

2.3. Deep Residual Dense Network (DRDN)

Deep Residual Dense Networks (DRDN) are deep learning architectures developed to improve the training capability of very deep neural networks. As network depth increases, conventional architectures may experience degraded learning performance due to gradient attenuation during backpropagation. DRDN mitigates this limitation by introducing residual connections that allow information to bypass intermediate layers and propagate directly to deeper layers (Wei et al., 2019). This residual learning mechanism improves gradient flow across the network and stabilizes training, enabling deeper architectures to learn more complex feature representations. Nonlinear activation functions are typically employed within residual blocks to enhance the model's representation capability, while optimization algorithms such as Adam are used to update network parameters during training (Musunuri et al., 2021). Owing to its ability to model highly nonlinear relationships and deep hierarchical structures, DRDN can improve classification accuracy on complex datasets.

2.4. Convolutional Neural Network - Long Short-Term Memory (CNN–LSTM)

The Convolutional Neural Network-Long Short-Term Memory (CNN-LSTM) model is a hybrid deep learning architecture that combines the strengths of CNNs and LSTMs to improve predictive performance on complex data structures (Nguyen et al., 2026). In this architecture, the CNN component first extracts representative spatial features and local patterns from the input data via convolutional operations. By applying a series of convolutional filters and nonlinear activation functions, CNN transforms the original input variables into higher-level feature representations that capture important spatial relationships among the conditioning factors. These extracted features are then passed to the LSTM component, which learns sequential dependencies and retains relevant information through its memory cell structure

and gating mechanisms. The LSTM network can model ordered or interdependent feature patterns by selectively preserving useful information and discarding less important signals during learning. As a result, the hybrid CNN–LSTM model can simultaneously exploit the spatial feature extraction capability of CNN and the sequence-learning capability of LSTM (Sainath et al., 2015).

By integrating these two architectures, the CNN–LSTM model provides a more flexible framework for learning complex nonlinear relationships in the dataset. This hybrid structure has been widely applied in prediction and classification problems where both local feature patterns and sequential dependencies are important for improving model performance.

2.5. Performance evaluation metrics

2.5.1. Area Under the Receiver Operating Characteristic Curve (AUC)

The area under the Receiver Operating Characteristic (ROC) curve (AUC) is widely used to evaluate the predictive performance of binary classification models (Xuan et al., 2024). The classification results are typically summarized in a confusion matrix with four components: True Positive (TP), True Negative (TN), False Positive (FP), and False Negative (FN). In land subsidence susceptibility mapping, TP represents correctly predicted subsidence locations, whereas TN denotes stable areas correctly classified as non-subsidence zones. Conversely, FP refers to stable locations incorrectly predicted as subsidence areas, and FN represents subsidence locations incorrectly classified as stable regions.

Based on these quantities, the predictive performance of the susceptibility model can be evaluated using the area under the Receiver Operating Characteristic Curve (AUC), which is calculated as:

$$AUC = \int_0^1 \mathrm{TPR(t)d(FPR(t))} \quad (1)$$

where the true positive rate (TPR) and false positive rate (FPR) are defined as:

$$\mathrm{TPR} = \frac{\mathrm{TP}}{\mathrm{TP + FN}} \quad (2)$$

$$\mathrm{FPR} = \frac{\mathrm{FP}}{\mathrm{FP + TN}} \quad (3)$$

The AUC value is calculated from the Receiver Operating Characteristic (ROC) curve, which plots the true positive rate (TPR) against the false positive rate (FPR) at different classification thresholds. The AUC ranges from 0 to 1 and reflects the model's overall ability to discriminate between subsidence-prone and stable locations (Cao et al., 2025). Higher AUC values indicate better predictive performance, whereas values close to 0.5 suggest that the model performs no better than random prediction. In general, models with AUC values greater than 0.8 are considered to have good predictive capability.

In addition to AUC analysis, model performance was further evaluated using several statistical metrics derived from the confusion matrix, including Accuracy (ACC), Positive Predictive Value (PPV), Negative Predictive Value (NPV), Sensitivity (SST), Specificity (SPF), Root Mean Square Error (RMSE), Mean Absolute Error (MAE), and the Kappa coefficient (Kumar et al., 2026). ACC represents the proportion of correctly classified samples among all observations, while PPV, NPV, SST, and SPF measure the model's ability to correctly predict positive samples, negative samples, subsidence locations, and stable areas, respectively. Higher values of these indicators indicate better classification performance. In addition, RMSE and MAE quantify the deviation between predicted and observed values; lower values indicate higher predictive accuracy. The Kappa coefficient measures the agreement between predicted and observed classifications while accounting for chance agreement, with values ranging from 0 to 1; higher values indicate stronger agreement and better model performance. The combined use

of these metrics provides a comprehensive evaluation of the classification accuracy and predictive reliability of the developed models.

2.5.2. Shapley Additive exPlanations (SHAP)

The Shapley Additive exPlanations (SHAP) method was used to interpret the contributions of individual input variables to model predictions. This method is derived from the concept of Shapley values in cooperative game theory and provides a unified framework for explaining complex machine learning models (Prakash et al., 2024). SHAP quantifies the influence of each input variable on the prediction by considering all possible feature combinations and calculating each variable's marginal contribution to the model's prediction. Consequently, this method enables a transparent and consistent interpretation of the role of individual variables in the prediction process. It provides locally accurate explanations for complex nonlinear models such as deep learning algorithms. The SHAP value of a feature represents its average contribution to the model prediction across all possible feature combinations; positive SHAP values indicate that the feature increases the predicted probability of the target event, whereas negative values indicate that the feature decreases the predicted probability.

Mathematically, the SHAP value for each feature is calculated as follows:

$$\phi_i = \sum_{S \subseteq N,\ \{i\}} \frac{|S|!(|N|-|S|-1)!}{|N|!}\left[f(S \cup \{i\}) - f(S)\right] \quad (4)$$

where N represents the complete set of input features, S denotes a subset of features that does not contain feature i, $|S|$ is the number of features in subset S, $f(S)$ represents the model prediction when only the features in subset S are considered, and $f(S \cup \{i\})$ denotes the model prediction when feature i is added to subset S. The term $f(S \cup \{i\}) - f(S)$ Therefore, it represents the marginal contribution of feature $i$to the model prediction.

In land subsidence studies, the SHAP method is applied to perform sensitivity analysis and to identify the relative influence of environmental and anthropogenic factors on ground surface subsidence processes (Hieu et al., 2026). By analyzing SHAP values, the study identifies the key controlling factors of land subsidence and clarifies the relationships between input variables and the susceptibility predictions generated by deep learning models. This analysis improves the interpretability of predictive models and provides scientific insights into mechanisms driving land subsidence, thereby supporting more reliable susceptibility assessments.

3. Study area

The study area is located in Hanoi City, between 20°53' and 21°23'N latitude and 105°44' and 106°02'E longitude, covering an area of approximately 3,359 km² (Fig. 1). The area borders Thai Nguyen Province to the north, Bac Ninh Province to the east, Hung Yen and Ninh Binh provinces to the south, and Phu Tho Province to the west.

The terrain is predominantly low-lying and relatively flat, with a deltaic plain mainly distributed across the city's central and southern parts. In contrast, hilly and mountainous terrains occur in the western and northwestern areas, particularly in Ba Vi and Soc Son districts. Geologically, most of Hanoi is underlain by young Quaternary alluvial sediments of Holocene and Pleistocene age, mainly consisting of clay, silt, and sand that are weakly consolidated. These sediments generally exhibit high porosity and compressibility, making the area susceptible to natural compaction and land surface subsidence under the influence of both natural and anthropogenic factors.

In addition, the study area lies within the hydrological system of the Red River, including its major tributaries, the Da, Duong, and Day rivers, which play an important role in sediment deposition and the formation of

deltaic geomorphology in the region. The variability in topographic, geological, and hydrological conditions, combined with rapid urbanization, intensive groundwater extraction, and increasing infrastructure loading, has significantly contributed to the occurrence and spatial distribution of land subsidence in the study area.

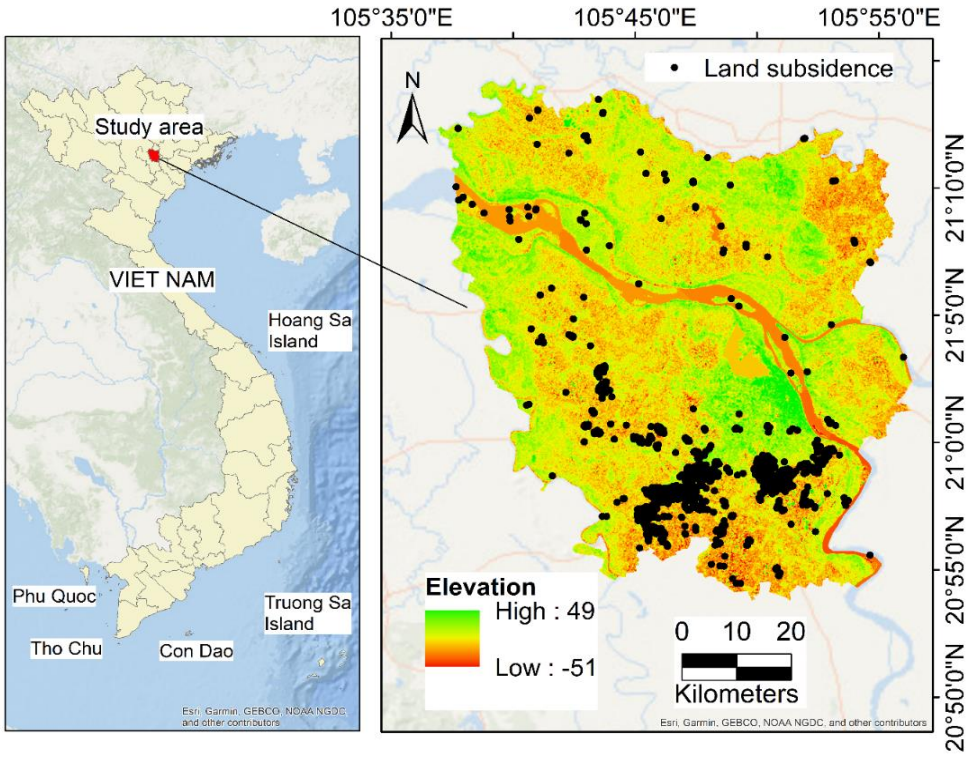

Figure 1. Location of the study area and distribution of land subsidence points

4. Data used

4.1. Land subsidence inventory

The land subsidence inventory dataset used in this study was developed from a time series of 22 raw L-band SAR scenes, acquired between February 2007 and February 2011 by the Japanese PALSAR sensor onboard the ALOS during its descending track 475, frame 400, and processed using a multi-temporal InSAR approach (Dang et al., 2014). As a result, 4,698 subsidence points were extracted to construct the land subsidence inventory dataset for the study area. This dataset was then used as input for training (70%) and validation (30%) of the models in the land subsidence susceptibility mapping process.

4.2. Conditioning factors

The conditioning factors used in this study include aspect, slope, curvature, elevation, normalized difference vegetation index (NDVI), groundwater, engineering geology, hydrogeology, Holocene sediment thickness, land use/land cover (LULC), rainfall, topographic wetness index (TWI), and Landsat 8 spectral bands 1–7 in Appendix A. These variables represent a combination of topographic, geological, hydrogeological, climatic, environmental, and remote-sensing factors that may influence ground deformation and land subsidence. The topographic parameters, including aspect, slope, curvature, elevation, and TWI, were derived from the ALOS PALSAR Digital Elevation Model

(DEM) provided by the United States Geological Survey (USGS) and made available through the Alaska Satellite Facility data portal. The NDVI and Landsat 8 Bands 1–7 were obtained from Landsat 8 satellite imagery downloaded from the USGS Earth Explorer platform. LULC information was also derived from satellite-based land-surface data. Rainfall data were collected from the Vietnam Meteorological and Hydrological Administration. In addition, thematic information related to groundwater, hydrogeology, engineering geology, and Holocene sediment thickness was compiled from available geological and hydrogeological maps and relevant national datasets. Finally, all thematic layers were resampled and standardized to a spatial resolution of 12.5 × 12.5 m to ensure consistency during spatial analysis and model development. To support the analysis and modeling process, these factors were further classified using the Natural Breaks (Jenks) method, which automatically defines class boundaries from the original data distribution; as a result, the class ranges may contain multiple decimal places while still better representing the spatial variability of each factor across the study area.

Slope represents the inclination of the terrain surface and influences drainage processes, erosion, and stress distribution within soil and rock layers. Areas with gentle slopes tend to favor the accumulation of water and sediments, which may increase the susceptibility to land subsidence. The slope map was classified into five classes: (-2.912659–2.912659)°, (2.912659–7.572913)°, (7.572913–16.310889)°, (16.310889–28.835321)°, and (28.835321–74.272797)°.

Aspect reflects variations in microclimatic conditions such as temperature, soil moisture, and vegetation distribution across different slope orientations. These variations can influence weathering processes, soil moisture conditions, and the stability of surface materials. The aspect map was classified into nine classes: Flat, North, Northeast, East, Southeast, South, Southwest, West, and Northwest.

Curvature provides information about terrain morphology and the distribution of surface runoff. Concave landforms tend to accumulate water and loose materials, whereas convex surfaces are more susceptible to erosion. The curvature map was classified into three classes: (-33.279999– -0.05), (-0.05–0.05), and (0.05–26.24).

Elevation influences climatic conditions, weathering processes, and the distribution of surface drainage systems. Areas at lower elevation tend to accumulate water and sediments, whereas higher areas are more strongly affected by erosion and weathering. The elevation map was classified into five classes: (-51– -21) m, (-21– -18) m, (-18– -15) m, (-15– -10) m, and (-10–49) m to analyze the spatial distribution of land subsidence.

The Normalized Difference Vegetation Index (NDVI) reflects the density and condition of vegetation cover. Areas with low NDVI values generally have sparse vegetation cover, making the ground surface more vulnerable to erosion, runoff, and terrain deformation processes. The NDVI map was classified into five classes: (-0.068686–0.034244), (0.034244–0.115659), (0.115659–0.171726), (0.171726–0.228846), and (0.228846–0.421462).

Groundwater is one of the most critical factors associated with land subsidence. Excessive groundwater extraction can reduce pore water pressure within soil layers, thereby inducing soil compaction and surface subsidence. In this study, the groundwater dataset comprised annual-average groundwater conditions for the period 2020–2025. The groundwater map was classified

into nine classes: (-22.363425– -14.48805), (-14.48805– -9.433705), (-9.433705– -4.614445), (-4.614445– -0.735529), (-0.735529–1.380243), (1.380243–2.673215), (2.673215–4.553902), (4.553902–6.317046), and (6.317046–7.727561).

Engineering geology is the study of the spatial distribution of subsurface materials with varying mechanical and geotechnical properties, such as strength, compressibility, and resistance to deformation. Variations in engineering geological conditions can strongly influence the ground's susceptibility to compaction and differential settlement, especially in areas underlain by weak or unconsolidated materials. The engineering geology map was classified into seven groups: Group 1 (rivers and lakes), Group 2 (brownish-gray to dark-gray mud containing organic matter and shells), Group 3 (sandy clay, clayey sand, upper sand, and lower gravelly sand containing small pebbles), Group 4 (filled soil and rock), Group 5 (a thin upper layer of sandy clay and clayey sand, underlain by sand containing gravel, cobbles, and small pebbles), Group 6 (sandy clay, clayey sandy silt, and upper sand, underlain by pebbles, gravelly pebbles, and sand containing sandy clay), and Group 7 (greenish-gray and mottled gray clay).

Hydrogeology reflects the occurrence, movement, and storage conditions of groundwater within the subsurface. Differences in hydrogeological conditions may control groundwater recharge, discharge, permeability, and the response of soil layers to changes in pore water pressure, thereby influencing ground deformation and land subsidence. The hydrogeology map was classified into five groups: Group 1 (Holocene aquifer), Group 2 (aquifer in the lower-middle Jurassic sediments of the Ha Coi Formation), Group 3 (Holocene aquitard composed of lower-middle marine, lagoonal, and marsh sediments of the Hai Hung Formation), Group 4 (Upper Pleistocene aquitard consisting of lagoonal, fluvial, and lacustrine sediments of the Vinh Phuc Formation), and Group 5 (rivers and lakes).

Holocene sediment thickness indicates The thickness of young unconsolidated sedimentary deposits. Areas with thicker Holocene sediments are generally more susceptible to compaction and deformation due to their relatively loose structure and weak consolidation state, which may increase the likelihood of land subsidence. The Holocene sediment thickness map was classified into five classes: (1.259564–5.822597), (5.822597–11.586429), (11.586429–17.95066), (17.95066–24.91529), and (24.91529–32).

Land Use/Land Cover (LULC) represents the spatial distribution of land use types and surface cover conditions. Human activities such as urbanization, infrastructure development, and land cover changes may alter soil stress conditions and increase the likelihood of land subsidence. The LULC map was classified into four categories: Agricultural land, Building land, River-pond-lake, and Vegetation.

Rainfall is an important climatic factor, that directly affects land subsidence processes. Rainwater infiltration can increase the pore water pressure and alter the stress conditions within soil layers, particularly in areas with weak or unconsolidated sediments. The rainfall map was classified into three classes: (1726.590961–1798.180613) mm, (1798.180613–1873.639976) mm, and (1873.639976–1974.25246) mm.

The Topographic Wetness Index (TWI) represents the potential for surface moisture accumulation across the terrain. High TWI values indicate areas with higher moisture retention capacity, which may increase soil saturation and promote compaction or deformation of weak soil layers. The TWI map was classified into five classes:

(1.385915–5.98798), (5.98798–7.785662), (7.785662–9.65525), (9.65525–11.524839), and (11.524839–19.72226).

Landsat 8 spectral bands 1–7 were used as supplementary remote sensing factors to provide multispectral information on the surface characteristics of the study area. These spectral bands reflect the spatial variability of surface reflectance, thereby helping distinguish areas with different surface conditions that may be related to ground deformation and land subsidence. In particular, Band 5 is a near-infrared band sensitive to vegetation condition, surface moisture, and land cover characteristics and may therefore indirectly reflect environmental conditions associated with land subsidence. In this study, each Landsat 8 band was classified into 5 classes to ensure consistency across the analysis.

5. Flowchart of the research framework

The overall research workflow adopted in this study is illustrated in Fig. 2, which summarizes the main steps for predicting land subsidence using multi-source data and deep learning models. The research framework consists of five main stages: (I) data collection and preparation, (II) data cleaning, (III) data preprocessing, (IV) model development and evaluation, and (V) land subsidence susceptibility mapping.

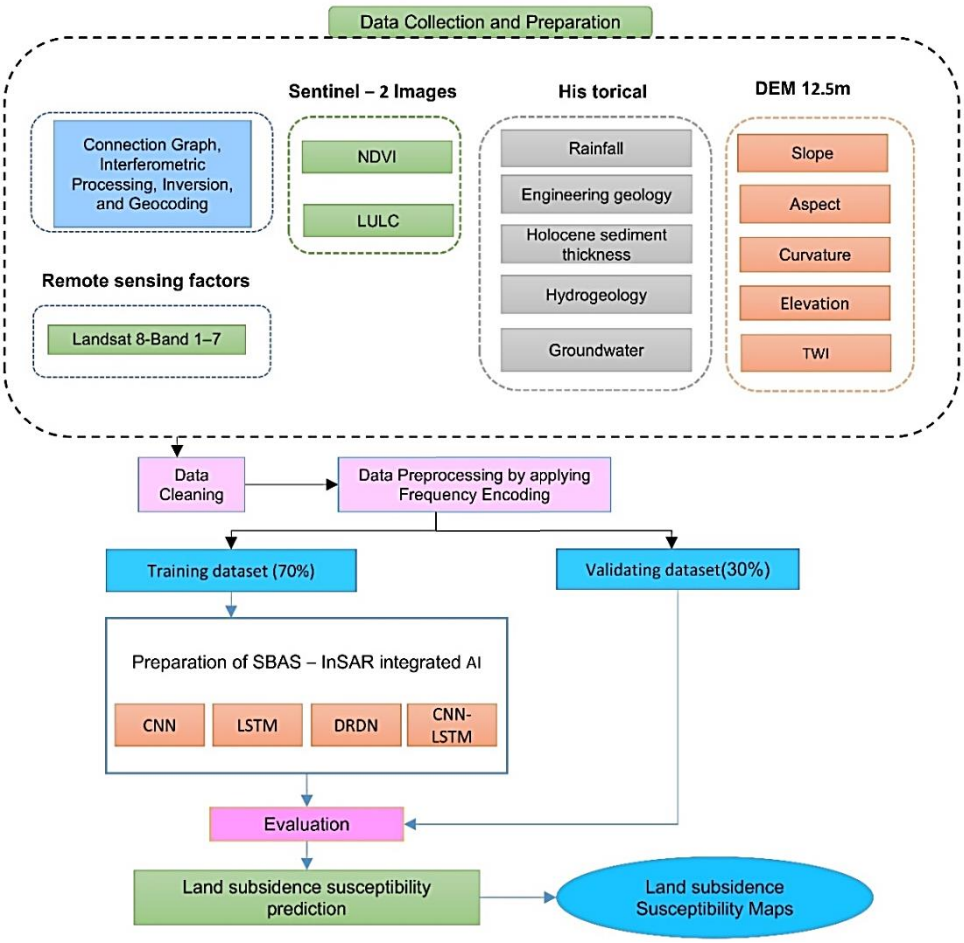

Figure 2. Methodological framework for land subsidence susceptibility

(i) Data were collected and integrated to construct the input dataset for land subsidence analysis. This dataset included Sentinel-1 radar images processed using the PS-InSAR technique to derive ground deformation information and identify subsidence locations. For the non-subsidence dataset, 3,997 points were randomly generated and distributed throughout the study area to represent areas without detected subsidence. In addition, the main conditioning factors were extracted and prepared in the ArcGIS 10.8 environment, including topographic factors (aspect, slope, curvature, elevation, and TWI), hydrogeological and geological factors (groundwater, hydrogeology, engineering geology, and Holocene sediment thickness), environmental and climatic factors (NDVI, LULC, and rainfall), and remote sensing factors represented by Landsat 8 spectral Bands 1–7.

(ii) The collected data were then subjected to data cleaning to ensure the consistency and reliability of the dataset. This process was performed using PyCharm 2023.2.5, including checking and removing missing values, correcting inconsistent records, and standardizing the data structure to ensure suitability for subsequent analysis and model development.

(iii) Data preprocessing was conducted to prepare the dataset for model construction and training. This step includes data normalization using the Min-Max normalization method (Mazziotta et al., 2022), correlation analysis of the input variables, and splitting the dataset into training and validation sets at 70% and 30%, respectively (Vrigazova, 2021). This ratio was selected because it has been widely used in predictive modeling studies and provides an effective balance between maximizing the available data for model training and retaining a sufficiently large validation subset for reliable validation.

The correlation analysis reveals the relationships among the conditioning factors used in the land subsidence prediction model (Fig. 3). The size and color of the circles indicate the magnitude and direction of the correlation coefficients. At the same time, the asterisks indicate the levels of statistical significance (*p ≤ 0.05, **p ≤ 0.01, ***p ≤ 0.001). Overall, correlations among most input variables are weak to moderate, whereas high correlations are observed only in several pairs of Landsat 8 spectral bands. Specifically, high correlations are found between Band 1 and Band 2 (r = 0.94), Band 3 and Band 4 (r = 0.87), Band 6 and Band 7 (r = 0.80), and between NDVI and Band 5 (r = 0.75). In addition, low correlations dominate among most of the remaining variables, indicating that the input factors generally provide complementary information for land subsidence prediction.

(iv) Deep learning models were then developed and trained, including Convolutional Neural Network (CNN), Long Short-Term Memory (LSTM), Deep Residual Dense Network (DRDN), and a hybrid CNN–LSTM model, to capture the nonlinear relationships between the conditioning factors and land subsidence. During the training process, Grid Search was employed to optimize the models' hyperparameters, and the resulting optimal configurations are presented in Appendix B. Model performance was evaluated using the area under the Receiver Operating Characteristic (ROC) curve (AUC), along with additional statistical indicators, to determine the best-performing model.

(v) Finally, the prediction results from the models were used to generate a land subsidence susceptibility map, which

represents the spatial distribution of areas with different levels of subsidence susceptibility. The mapping and visualization process was performed in ArcGIS 10.8, where the model predictions were converted to raster layers and classified into different susceptibility levels.

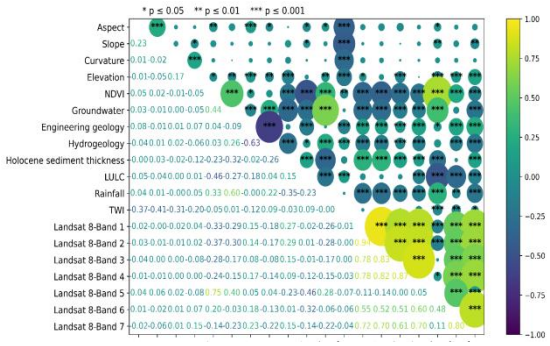

Figure 3. Correlation matrix of land subsidence conditioning factors with statistical significance levels

6. Results and discussion

6.1. Performance evaluation of the model

Evaluation of the models based on AUC values reveals clear differences in predictive performance among the models in both the training and validation datasets (Fig. 4). For the training dataset, the DRDN model achieves the best performance with the highest AUC value of 0.984, indicating an excellent ability to distinguish between subsidence-prone and stable areas. The LSTM model also performs strongly with an AUC of 0.962, followed by the CNN model (AUC = 0.931) and the CNN-LSTM model (AUC = 0.924). The ROC curves for DRDN and LSTM are generally closer to the upper-left corner of the graph, indicating higher sensitivity and lower false-positive rates than those of the other models. On the validation dataset, the DRDN model again achieves the best predictive performance, with an AUC of 0.957, confirming its strong generalization capability. The LSTM model ranks second with an AUC of 0.952, while the CNN and CNN-LSTM models achieve AUC values of 0.927 and 0.921, respectively. Although the AUC values in the testing stage are slightly lower than those in the training stage, all models still maintain good predictive performance, with AUC values above 0.92. Overall, the AUC analysis indicates that the DRDN model outperforms the other models across both datasets, demonstrating its superior ability to capture the complex, nonlinear relationships underlying land subsidence prediction.

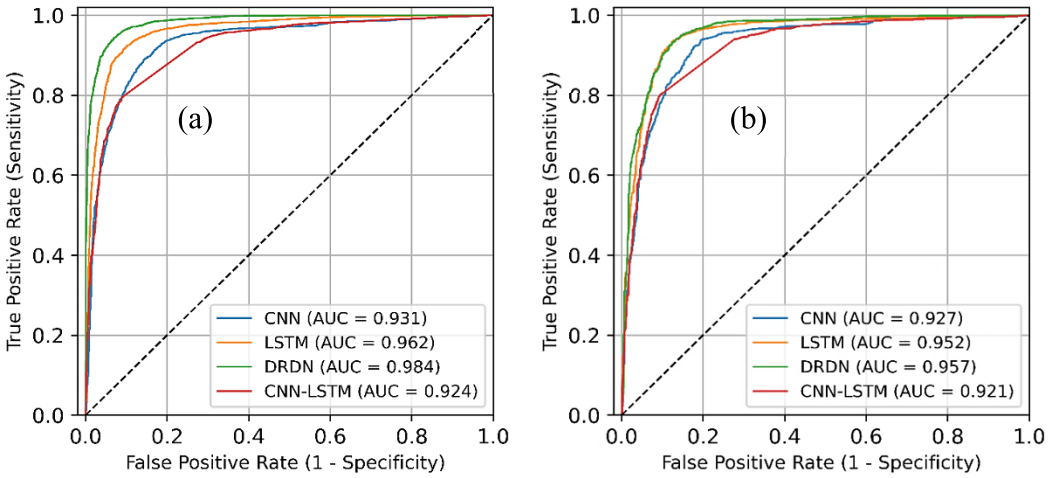

Figure 4. AUC analysis of the models using training and validation datasets

During the training phase, the models' performance was evaluated according to Table 1. The results show that the DRDN model outperformed the other models in most evaluation metrics. Specifically, DRDN achieved the highest number of true positives (TP = 3173) and true negatives (TN = 2521), while also producing the lowest number of false positives (FP = 274) and false negatives (FN = 118). By comparison, the CNN, LSTM, and CNN-LSTM models yielded TP values of 3008, 3047, and 3069, and TN values of 2315, 2494, and 2033, respectively. In terms of predictive metrics, DRDN recorded the highest PPV (92.05%), NPV (95.53%), sensitivity (SST = 96.41%), specificity (SPF = 90.20%), and overall accuracy (ACC = 93.56%). It also obtained the highest Kappa coefficient (0.87), indicating the strongest agreement between predicted and observed results. In addition, DRDN produced the lowest error values, with MAE = 0.064 and RMSE = 0.254. These findings confirm that DRDN achieved the best overall performance during training.

Table 1. Accuracy analysis of the models

	Training datasets				**Validation datasets**			
	CNN	**LSTM**	**DRDN**	**CNN-LSTM**	**CNN**	**LSTM**	**DRDN**	**CNN-LSTM**
TP	3008	3047	3173	3069	1293	1333	1315	1324
TN	2315	2494	2521	2033	991	1028	1051	857
FP	480	301	274	762	211	174	151	345
FN	283	244	118	222	114	74	92	83
PPV (%)	86.24	91.01	92.05	80.11	85.97	88.45	89.7	79.33
NPV (%)	89.11	91.09	95.53	90.16	89.68	93.28	91.95	91.17
SST (%)	91.4	92.59	96.41	93.25	91.9	94.74	93.46	94.1
SPF (%)	82.83	89.23	90.2	72.74	82.45	85.52	87.44	71.3
ACC (%)	87.46	91.05	93.56	83.83	87.54	90.49	90.69	83.6
Kappa	0.746	0.819	0.87	0.67	0.748	0.808	0.812	0.665
MAE	0.125	0.09	0.064	0.162	0.125	0.095	0.093	0.164
RMSE	0.354	0.299	0.254	0.402	0.353	0.308	0.305	0.405

For the validation dataset, the DRDN model remained the best-performing model overall. It achieved the highest TN (1051), the lowest FP (151), the highest PPV (89.70%), specificity (87.44%), overall accuracy (ACC = 90.69%), and Kappa coefficient (0.812), while also producing the lowest prediction errors, with MAE = 0.093 and RMSE = 0.305. The LSTM model also showed strong performance, achieving the highest NPV (93.28%) and sensitivity (94.74%), together with ACC = 90.49% and Kappa = 0.808, which were only slightly lower than those of DRDN. By comparison, the CNN model showed moderate performance, whereas the CNN–LSTM model produced the weakest overall results, with ACC = 83.60%, Kappa = 0.665, MAE = 0.164, and RMSE = 0.405. Therefore, given its highest AUC and strongest performance on the validation dataset, DRDN was identified as the most reliable and best-performing model.

Additionally, the comparison of Mean Absolute Error (MAE±STD) for the four models CNN, LSTM, DRDN, and CNN-LSTM on the validation dataset is presented in Fig. 5. The results reveal clear differences in model performance. Among the evaluated models, DRDN achieves the lowest MAE (0.138±0.235), indicating the highest predictive accuracy and stronger ability to capture the nonlinear relationships between environmental factors and land subsidence. The LSTM model ranks second, with a MAE of 0.152±0.229, demonstrating relatively good predictive performance. In contrast, the

CNN–LSTM hybrid model records the highest MAE (0.235±0.234), while the CNN model also shows a relatively high MAE (0.205 ± 0.241), suggesting that the CNN–LSTM configuration does not significantly improve prediction accuracy in this study.

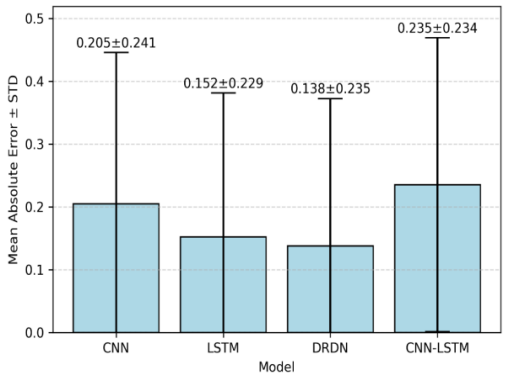

Figure 5. Comparison of Mean Absolute Error (MAE ± STD) of the four models on the validation dataset

The distribution of absolute prediction errors of the DRDN model in both the training dataset (a) and the validation dataset (b) is illustrated using histograms combined with cumulative frequency curves (Fig. 6). Since the target variable is binary (0 and 1), the absolute prediction errors naturally range between 0 and 1. In both datasets, a considerable proportion of samples exhibit very small error values (approximately 0–0.1), indicating that many predicted probabilities are close to the observed labels. However, a noticeable number of samples are also concentrated in the high-error range near 0.9–1.0, whereas the intermediate error levels occur less frequently. The cumulative frequency curves increase gradually across the low- and mid-error intervals and then rise more sharply in the upper error range, especially from about 0.8 to 1.0.

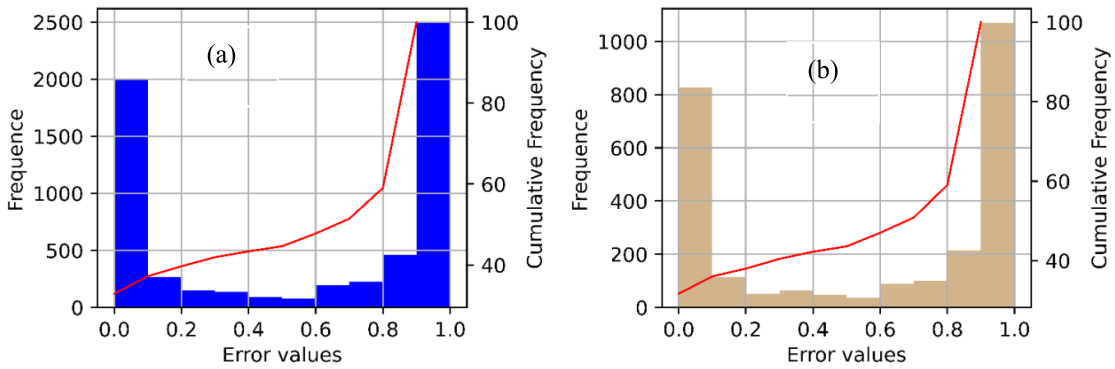

Figure 6. Distribution of prediction errors for land subsidence modeling: (a) training dataset and (b) validation dataset

The mean SHAP value plot illustrating the influence of input factors on the prediction of land subsidence susceptibility is shown in Fig. 7. The factors are ranked in descending order by the mean absolute SHAP value (mean |SHAP value|), with higher values indicating a greater contribution to the model prediction. The results show that Holocene sediment thickness is the most influential factor, with a mean SHAP value of approximately +0.11, highlighting the important role of unconsolidated young sediments in land subsidence. This is followed by groundwater, with a mean SHAP value of about +0.10, confirming the strong influence of hydrogeological conditions on subsidence processes. Landsat 8-Band 5 and engineering geology both show mean SHAP values of

approximately +0.06, suggesting a notable contribution from spectral surface characteristics and subsurface material properties. In addition, hydrogeology has a mean SHAP value of about +0.04, while Landsat 8 Band 7 has a value of approximately +0.03, indicating a moderate influence on model predictions. The factors Landsat 8-Band 2, Landsat 8-Band 4, LULC, aspect, and rainfall each exhibit mean SHAP values of around +0.02, whereas Landsat 8-Band 3 has a mean SHAP value of approximately +0.01, suggesting a lower but still noticeable contribution to the prediction process. Meanwhile, the remaining seven factors, including slope, curvature, elevation, NDVI, TWI, Landsat 8-Band 1, and Landsat 8-Band 6, collectively contribute about +0.07, indicating that their individual effects are relatively limited compared with the leading variables in the land subsidence prediction model.

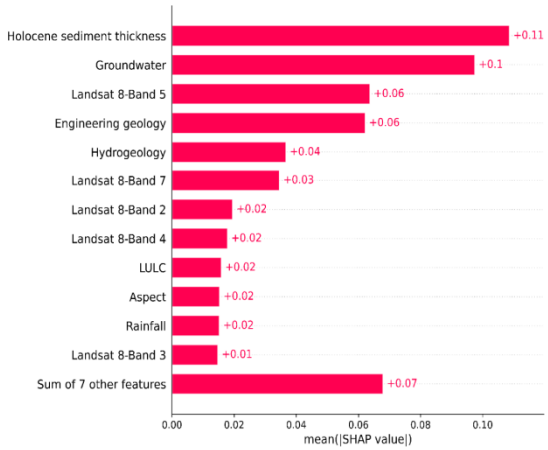

Figure 7. Feature importance for land subsidence prediction based on mean(|SHAP value|)

In addition to analyzing mean SHAP values, the SHAP method also enables a detailed evaluation of each input factor's contribution to the model prediction through the SHAP waterfall plot, which illustrates how individual features contribute to the final model output for a specific sample. The results shown in Fig. 8 indicate that the final predicted value of the model is approximately 0.002, obtained from the baseline model expectation E[f(x)] = 0.582 after summing the contributions of the input features. Among them, groundwater has the strongest negative influence, with a SHAP value of approximately -0.25, followed by Landsat 8-Band 7 and Landsat 8-Band 5, each with a SHAP value of approximately -0.07. Rainfall, Landsat 8 Band 2, Elevation, NDVI, and Hydrogeology also reduce the predictive value, with SHAP values of approximately -0.06, -0.05, -0.04, -0.03, and -0.02, respectively. In contrast, Landsat 8-Band 4 and Engineering geology slightly increase the prediction value, each with a SHAP value of about +0.02. Other factors, including Landsat 8-Band 3, Curvature, Holocene sediment thickness, TWI, Slope, LULC, Aspect, Landsat 8-Band 6, and Landsat 8-Band 1, have very small SHAP values, indicating a limited influence on the prediction result for the analyzed sample.

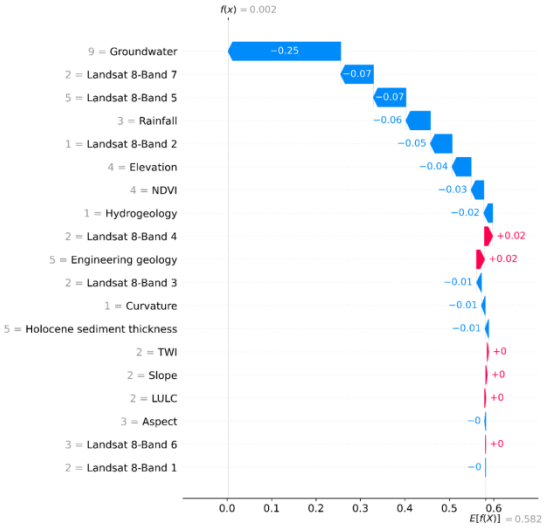

Figure 8. SHAP waterfall plot showing feature contributions to the model output

SHAP dependence plots with ICE curves were used to further the nonlinear relationships between conditioning factors and land subsidence prediction (Appendix C). In these plots, the thin lines represent ICE curves, illustrating how the model output changes for individual samples as each feature varies across its classes. The results show that Groundwater, Engineering geology, Hydrogeology, Holocene sediment thickness, and several Landsat 8 spectral bands exhibit noticeable variations in predicted values, indicating a strong influence on the model prediction. In particular, groundwater shows a clear decreasing trend at higher classes. In contrast, Holocene sediment thickness and Engineering geology display pronounced increasing trends, suggesting that these factors play important roles in controlling land subsidence susceptibility. Among the spectral variables, Landsat 8-Band 5 shows a marked decrease, while Landsat 8-Band 7 shows an increase, highlighting their nonlinear contributions to the model output. NDVI, Elevation, Hydrogeology, LULC, and Rainfall also show moderate variations in the predicted values across their ranges, suggesting a secondary but still meaningful influence on land subsidence prediction. In contrast, topographic factors such as Aspect, Slope, Curvature, and TWI display relatively small changes in predicted values, indicating a more limited contribution to the model output. Overall, the SHAP dependence plots with ICE curves indicate that hydrogeological, geological, sedimentary, and spectral factors play a more dominant role in controlling land subsidence prediction than several topographic variables in the study area.

6.2. Land subsidence susceptibility mapping

6.2.1. Development of the land subsidence susceptibility map

The land subsidence susceptibility map is a spatial product that represents the likelihood of land subsidence occurring at specific locations within the study area, playing an important role in identifying and classifying zones with susceptibility levels ranging from very low to very high. To construct this map, the model's prediction results were exported as a data table (.xls), with each record containing geographic coordinates (X, Y) and the corresponding subsidence susceptibility value. The data were then imported into ArcGIS 10.8 as a point layer and subsequently converted into a raster grid using the "Point to Raster" tool to generate a continuous spatial surface representing the distribution of land subsidence susceptibility across the study area.

The raster dataset was classified into five land subsidence susceptibility levels using the Natural Breaks (Jenks) method, which determines class boundaries by minimizing the variance within each class. The classification results show that land subsidence susceptibility was divided into five categories: very low (0.000000–0.078125), low (0.078125–0.249999), moderate (0.249999–0.507811), high (0.507811–0.781248), and very high (0.781248–0.999998) (Fig. 9). The susceptibility map clearly illustrates the spatial distribution of potential land subsidence within the study area, with high and very high susceptibility zones mainly concentrated in the southern and southeastern parts, whereas low and very low susceptibility classes are more widely distributed across the remaining areas.

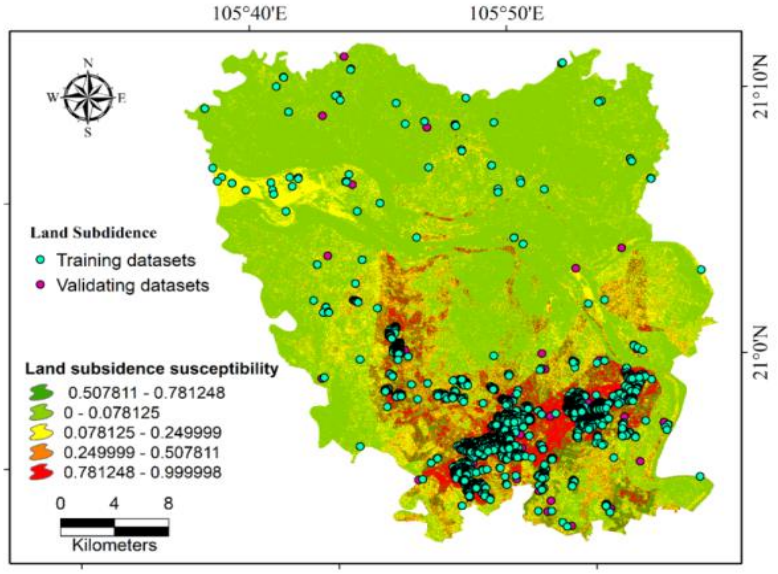

Figure 9. Land subsidence susceptibility map generated by the DRDN model

6.2.2. Accuracy assessment of the land subsidence susceptibility map

The accuracy of the land subsidence susceptibility map was evaluated using the Frequency Ratio (FR) method by comparing the percentage of subsidence occurrences within each susceptibility class with the percentage of the area occupied by that class across the entire study region (Table 2). The results indicate that 85.43% of the observed land subsidence points are concentrated in the very high susceptibility class. In comparison, 8.81% occur in the high susceptibility class, and only 5.75% are distributed within the remaining three lower susceptibility classes. This finding indicates that most subsidence events occur in areas predicted by the model as having high or very high susceptibility.

Table 2. Density analysis of land subsidence across susceptibility classes derived from the DRDN model

Class	Pixels of class	Pixels of land subsidence	Frequency ratio	Percentage of classified pixels	Percentage of land subsidence pixels
0–0.078125	3507535	22	0.025	63.7	1.56
0.078125–0.249999	807093	10	0.048	14.66	0.71
0.249999–0.507811	420844	49	0.456	7.64	3.48
0.507811–0.781248	364452	124	1.332	6.62	8.81
0.781248–0.999998	406802	1202	11.564	7.39	85.43

A more detailed analysis shows that the very high susceptibility class (0.781248–0.999998) occupies only 7.39% of the total area but contains 1,202 subsidence points, yielding a frequency ratio (FR) value of 11.564, which indicates a strong correlation between the predicted very high susceptibility zones and the actual occurrence of land subsidence. In contrast, the very low susceptibility class (0–0.078125) covers 63.70% of the study area. Still, it accounts for only 1.56% of the subsidence points, with an FR value of 0.025, indicating a very low likelihood of subsidence in these areas. The low- and moderate-susceptibility classes also exhibit FR values below 1, indicating a weak relationship between these zones and land subsidence.

These results indicate that the land subsidence susceptibility map generated by the deep learning model can effectively classify and predict the spatial distribution of subsidence-prone areas in Hanoi. Compared with the study of (Arnhardt et al., 2023), which is the closest previous work in terms of susceptibility mapping in Hanoi and reported an AUC of about 0.7 based mainly on geological factors, the present study demonstrates stronger predictive capability through the integration of a multi-temporal InSAR approach -derived subsidence inventory and a more comprehensive set of conditioning factors. Previous studies using ALOS InSAR (Dang et al., 2014), TerraSAR-X (Le et al., 2016), Sentinel-1A (Bui et al., 2021), multi-sensor InSAR analysis (Zhao et al., 2025), and finite element modeling have consistently shown that subsidence is mainly concentrated in the southern and western parts of Hanoi, particularly in Ha Dong, Hoai Duc, Thanh Tri, and Hoang Mai, while some areas north of the Red River or in the historic urban core remain relatively stable. These studies further indicate that groundwater exploitation, geological conditions, Holocene sediment thickness, and construction or urbanization activities are among the major factors influencing land subsidence. On that basis, the present study not only confirms previously reported spatial patterns and controlling factors, but also improves their practical interpretation by directly quantifying subsidence susceptibility using a deep learning framework, thereby offering a clearer and more reliable spatial assessment of subsidence risk.

7. Concluding remarks

The results of this study indicate that integrating a multi-temporal InSAR technique with deep learning models is an effective approach for predicting land subsidence susceptibility. Among the evaluated models, the DRDN model achieved the best overall performance, with the highest AUC values, demonstrating superior capability in classifying and predicting land subsidence susceptibility compared with the CNN, LSTM, and CNN-LSTM models. Based on this optimal model, a land subsidence susceptibility map was generated, and the study area was classified into five susceptibility levels. The evaluation results show that 85.43% of the observed subsidence points are located within the very high susceptibility zone and 8.81% within the high susceptibility zone, indicating a strong agreement between the model predictions and the actual subsidence occurrences. However, this study still has several limitations, including the use of point-based subsidence data rather than areal (polygon-based) representations, and the reliance on conditioning factors derived from single time points rather than time-series data, which may not fully capture the spatial characteristics and temporal variability of land subsidence. Another important limitation of this study is that the land subsidence inventory and related influencing factors were compiled from datasets available at the time of analysis and may therefore not fully reflect current subsidence conditions in the study area. Future research should focus on continuously updating the subsidence database using newly acquired multi-temporal InSAR observations, recent field survey data, and real-time or near-real-time monitoring information.

Acknowledgments

We are grateful to Dr. Vu Van Ha, Dr. Dinh Van Thuan, and Prof. Pham Qui Nhan for sharing the data used in this research.

Conflict of Interest

The authors declare no conflicts of interest.

Funding

The University of Transport Technology funds this research under the project entitled "Assessment of land subsidence susceptibility using artificial intelligence technology

integrated with geospatial techniques", grant number ĐTTĐ2023-19.

References

Abidin H.Z., Djaja R., Darmawan D., Hadi S., Akbar A., Rajiyowiryono H., Sudibyo Y., Meilano I., Kasuma M.A., Kahar J., Subarya C., 2001. Land subsidence of Jakarta (Indonesia) and its geodetic monitoring system. Natural Hazards, 23(2), 365−387. https://doi.org/10.1023/A:1011144602064.

Ahmed S.F., Alam M.S.B., Hassan M., Rozbu M.R., Ishtiak T., Rafa N., Mofijur M., Shawkat Ali A.B.M., Gandomi A.H., 2023. Deep learning modelling techniques: current progress, applications, advantages, and challenges. Artificial Intelligence Review, 56(11), 13521−13617. https://doi.org/10.1007/s10462-023-10466-8.

Arnhardt R., Novellino A., Hussain E., Bateson L., Newell A., 2023. Land subsidence susceptibility mapping for Hanoi city, Vietnam. Paper presented at the Tenth International Symposium on Land Subsidence. https://nora.nerc.ac.uk/id/eprint/536209.

Bui L.K., Le P.V., Dao P.D., Long N.Q., Pham H.V., Tran H.H., Xie L., 2021. Recent land deformation detected by Sentinel-1A InSAR data (2016–2020) over Hanoi, Vietnam, and the relationship with groundwater level change. GIScience & Remote Sensing, 58(2), 161−179. https://doi.org/10.1080/15481603.2020.1868198.

Cao D.V., Thanh N.P.T., Hong T.T., Van P.T., Van K.M., Van D.H., Indra Prakash, Pham B.T., 2025. Novel Integration of JCHAIDStar with ensemble techniques for comprehensive landslide and flash flood susceptibility mapping. Vietnam Journal of Earth Sciences, 48(2), 219−238. https://doi.org/10.15625/2615-9783/24030.

Chai L., Wei L., Cai P., Liu J., Kang J., Zhang Z., 2024. Risk assessment of land subsidence based on GIS in the Yongqiao area, Suzhou City, China. Scientific Reports, 14(1), 11377. https://doi.org/10.1038/s41598-024-62108-w.

Dang V., Doubre C., Weber C., Gourmelen N., Masson F., 2014. Recent land subsidence caused by the rapid urban development in the Hanoi region (Vietnam) using ALOS InSAR data. Natural Hazards and Earth System Sciences, 14(3), 657−674. https://doi.org/10.5194/nhess-14-657-2014.

Dang V.K.K., Nguyen H.T., Au T.A., Pham T.H., 2022. Deep based learning: ebin sorting system development. Vietnam Journal of Marine Science and Technology, 22(1), 85–93. https://doi.org/10.15625/1859-3097/16928.

Eghbali M., Azarakhshi M., Khalaj M.R., 2024. Determining land subsidence potential using the evidential belief function model: A case study for the Bardaskan Aquifer, Iran. Natural Resource Modeling, 37(3), e12397. https://doi.org/10.1111/nrm.12397.

Faryabi M., 2023. A fuzzy logic approach for land subsidence susceptibility mapping: the use of hydrogeological data. Environmental Earth Sciences, 82(9), 209. https://doi.org/10.1007/s12665-023-10909-z.

Galloway D.L., Burbey T.J., 2011. Regional land subsidence accompanying groundwater extraction. Hydrogeology Journal, 19(8), 1459−1486. https://doi.org/10.1007/s10040-011-0775-5.

Hieu T.T., Cham D.D., Van Tien P., Quan N.C., Hai P.T., Anh N.D., Thao P.B., Van T.T.T, Trinh Q.N., Thanh N.T., Cuong T.Q., 2026. Landslide detection and susceptibility analysis: A case study in Pieng stream catchment, Son La province. Journal of Science and Transport Technology, 6(1), 282−299. https://doi.org/10.58845/jstt.utt.2026.en.6.1.282-299.

Holzer T.L., Galloway D.L., 2005. Impacts of land subsidence caused by withdrawal of underground fluids in the United States. https://doi.org/10.1130/2005.4016(08).

Hong S.-H., 2024. Monitoring Time-Series Subsidence Observation in Incheon Using X-Band COSMO-SkyMed Synthetic Aperture Radar. Korean Journal of Remote Sensing, 40(2), 141−150. https://doi.org/10.7780/kjrs.2024.40.2.2.

Hosseinzadeh E., Anamaghi S., Behboudian M., Kalantari Z., 2024. Evaluating Machine Learning-Based Approaches in Land Subsidence Susceptibility Mapping. Land, 13(3), 322, https://doi.org/10.3390/land13030322.

Ikehara M.E., Phillips S.P., 1994. Determination of land subsidence related to ground-water-level declines using global positioning system and leveling surveys in Antelope Valley, Los Angeles and Kern Counties, California, 1992 (vol. 94): US Department of the Interior, US Geological Survey.

Karimiasl S., Hessari B., Zeinalzadeh K., Erfanian M., 2024. Assessment of land subsidence susceptibility in the Salmas Plain Aquifer Northwestern Lake Urmia, utilizing fuzzy logic. Watershed Engineering and Management, 16(3), 331−353.

Kariminejad N., Mohammadifar A., Sepehr A., Garajeh M.K., Rezaei M., Desir G., Román Q.A., Gholami H., 2024. Detection of land subsidence using hybrid and ensemble deep learning models. Applied Geomatics, 16(3), 593−610, https://doi.org/10.1007/s12518-024-00572-9.

Ku C.-Y., Liu C.-Y., 2023. Modeling of land subsidence using GIS-based artificial neural network in Yunlin County, Taiwan. Scientific Reports, 13(1), 4090. https://doi.org/10.1038/s41598-023-31390-5.

Kumar R., Ha H., Son N.D., Nguyen L.H., 2025. Optimizing CNN, SVM, and MLP for Prediction of Compressive Strength of Concrete using Grid Search Optimization. Journal of Science and Transport Technology, 198−217. https://doi.org/10.58845/jstt.utt.2025.en.5.4.198-217.

Le T.S., Chang C.-P., Nguyen X.T., Yhokha A., 2016. TerraSAR-X data for high-precision land subsidence monitoring: A case study in the historical centre of Hanoi, Vietnam. Remote Sensing, 8(4), 338. https://doi.org/10.3390/rs8040338.

Lenardón Sánchez M., Farías C.A., Cigna F., 2024. Multi-Decadal Land Subsidence Risk Assessment at Major Italian Cities by Integrating PSInSAR with Urban Vulnerability. Land, 13(12), 2103. https://doi.org/10.3390/land13122103.

Li F., Liu G., Tao Q., Zhai M., 2023. Land subsidence prediction model based on its influencing factors and machine learning methods. Natural Hazards, 116(3), 3015−3041. https://doi.org/10.1007/s11069-022-05796-9.

Liu K., Zhang J., Liu J., Wang M., Yue Q., 2024. Projection of land susceptibility to subsidence hazard in China using an interpretable CNN deep learning model. Science of the Total Environment, 913, 169502. https://doi.org/10.1016/j.scitotenv.2023.169502.

Liu X., Chen H., Gong B., Jiang G., Wang J., 2024. Formation process of cover collapse sinkholes related to groundwater level decline in karst areas. Journal of Mountain Science, 21(11), 3832−3846. https://doi.org/10.1007/s11629-024-8944-x.

Massonnet D., Feigl K.L., 1995. Discrimination of geophysical phenomena in satellite radar interferograms. Geophysical Research Letters, 22(12), 1537−1540. https://doi.org/10.1029/95GL00711.

Massonnet D., Feigl K.L., 1998. Radar interferometry and its application to changes in the Earth's surface. Reviews of geophysics, 36(4), 441−500. https://doi.org/10.1029/97RG03139.

Mazziotta M., Pareto A., 2022. Normalization methods for spatio-temporal analysis of environmental performance: Revisiting the Min-Max method. Environmetrics, 33(5), e2730. https://doi.org/10.1002/env.2730.

Mehrnoor S., Robati M., Kheirkhah Zarkesh M.M., Farsad F., Baikpour S., 2023. Land subsidence hazard assessment based on novel hybrid approach: BWM, weighted overlay index (WOI), and support vector machine (SVM). Natural Hazards, 115(3), 1997−2030. https://doi.org/10.1007/s11069-022-05624-0.

Musunuri Y.R., Kwon O.-S., 2021. Deep residual dense network for single image super-resolution. Electronics, 10(5), 555. https://doi.org/10.3390/electronics10050555.

Nguyen T.G., Tran T.D., Nguyen C.T., 2023. A Optimizing the Long Short-Term Memory (LSTM) model by Bayesian method for salinity intrusion forecasting: a study at Dai Ngai station, Soc Trang province, Vietnam. Vietnam Journal of Marine Science and Technology, 23(3), 223−232. https://doi.org/10.15625/1859-3097/18174.

Nguyen T.D., Ha Q.M., Truong K.H., Cu M.H., Nguyen V.H., 2024. Applying machine learning for hydraulic flow unit classification and permeability prediction: case study from carbonate reservoir in the Southern part, Song Hong basin. Vietnam Journal of Marine Science and Technology, 24(3), 219−234. https://doi.org/10.15625/1859-3097/18654.

Nguyen H.D., Dinh K.D., Truong H.Q., Bui Q.-T., Nguyen T.N.U., Petrisor A.-I., 2025. Flood susceptibility assessment using deep neural networks and open-source spatial datasets in transboundary river basin. Vietnam Journal of Earth Sciences, 47(3), 315−336. https://doi.org/10.15625/2615-9783/22711.

Nguyen T.-H., Le V.-H., 2026. Cross-Branch CNN-MLP Integration for Improving Landslide Spatial Probability on Mt. Umyeon, Korea. Journal of Science and Transport Technology, 183−198. https://doi.org/10.58845/jstt.utt.2026.en.6.1.183-198.

Nozadkhalil T., Cakir Z., Ergintav S., Doğan U., Walter T.R., 2023. Land subsidence due to natural gas extraction in the Thrace basin (NW Turkey) and its influence on the North Anatolian fault under the Marmara Sea. Turkish Journal of Earth Sciences, 32(3), 421−430. https://doi.org/10.55730/1300-0985.1852.

Pan Z., Chen X., Yang X., Song Y., Ban R., Zhang M., 2022. Formation mechanism analysis of cover

collapse sinkholes in Wugaishan Town, Chenzhou City, Hunan province, China. Environmental Earth Sciences, 81(2), 48. https://doi.org/10.1007/s12665-022-10171-9.

Pham G.H., Pham B.T.T., Hoang K.O.T., Tran T.T., Chi H.N.D., 2026. GIS Based Soil Erosion Susceptibility Assessment Using Deep Learning Models: A Case Study in the Mountainous Region of Nghe An, Vietnam. Journal of Science and Transport Technology, 67−86. https://doi.org/10.58845/jstt.utt.2026.en.6.1.67-86.

Prakash I., Nguyen D.D., Tuan N.T., Van Phong T., Van Hiep L., 2024. Landslide susceptibility zoning: integrating multiple Intelligent models with SHAP Analysis. Journal of Science and Transport Technology, 23−41. https://doi.org/10.58845/jstt.utt.2024.en.4.1.23-41.

Sainath T.N., Vinyals O., Senior A., Sak H., 2015. Convolutional, long short-term memory, fully connected deep neural networks. In 2015 IEEE international conference on acoustics, speech and signal processing (ICASSP). Ieee, 4580−4584. Doi: 10.1109/ICASSP.2015.7178838.

Sekkeravani M.A., Bazrafshan O., Pourghasemi H.R., Holisaz A., 2022. Spatial modeling of land subsidence using machine learning models and statistical methods. Environmental Science and Pollution Research, 29(19), 28866−28883. https://doi.org/10.1007/s11356-021-18037-6.

Sun H., Peng H., Zeng M., Wang S., Pan Y., Pi P., Xue Z., Zhao X., Zhang A., Liu F., 2023. Land subsidence in a coastal city based on SBAS-InSAR monitoring: a case study of Zhuhai, China. Remote sensing, 15(9), 2424. https://doi.org/10.3390/rs15092424.

Teatini P., Tosi L., Strozzi T., Carbognin L., Wegmüller U., Rizzetto F., 2005. Mapping regional land displacements in the Venice coastland by an integrated monitoring system. Remote sensing of environment, 98(4), 403−413. https://doi.org/10.1016/j.rse.2005.08.002.

Tuan T., Hong P., Tam T., Nguyet N., Dung N., Huy P., Phong T., 2024. Landslide susceptibility in Phuoc Son, Quang Nam: A deep learning approach. Vietnam Journal of Earth Sciences, 47(1), 39−57. https://doi.org/10.15625/2615-9783/21658.

Vrigazova B., 2021. The proportion for splitting data into training and test set for the bootstrap in classification problems. Business Systems Research: International Journal of the Society for Advancing Innovation and Research in Economy, 12(1), 228−242. https://doi.org/10.2478/bsrj-2021-0015

Wei W., Yongbin J., Yanhong L., Ji L., Xin W., Tong Z., 2019. An advanced deep residual dense network (DRDN) approach for image super-resolution. International Journal of Computational Intelligence Systems, 12(2), 1592−1601. https://doi.org/10.2991/ijcis.d.191209.001.

Wu J., Shi X., Ye S., Xue Y., Zhang Y., Wei Z., Fang Z., 2010. Numerical simulation of viscoelastoplastic land subsidence due to groundwater overdrafting in Shanghai, China. Journal of Hydrologic Engineering, 15(3), 223−236. https://doi.org/10.1061/(ASCE)HE.1943-5584.0000172.

Xuan B.T., Thuy D.L., Van P.T., Hong N.V., Van Le H., Nguyen D.D., Prakash I., Thanh T.P., Thai B.P., 2024. Groundwater potential zoning using Logistics Model Trees based novel ensemble machine learning model. Vietnam Journal of Earth Sciences, 46(2), 272−281. https://doi.org/10.15625/2615-9783/20316.

Younas M., Khan S.D., Tirmizi O., Hamed Y., 2023. Geospatial analytics of driving mechanism of land subsidence in Gulf Coast of Texas, United States. Science of the Total Environment, 902, 166102. https://doi.org/10.1016/j.scitotenv.2023.166102.

Yu H., Arabameri A., Costache R., Crăciun A., Arora A., 2022. Land subsidence susceptibility assessment using advanced artificial intelligence models. Geocarto International, 37(27), 18067−18093. https://doi.org/10.1080/10106049.2022.2136265.

Zebker H., Villasenor J., 1992. Decorrelation in interferometric radar echoes. IEEE Transactions on geoscience and remote sensing, 30(5), 950−959.

Zhao Q., Zhang Y., Pepe A., Mastro P., Zheng T., Yang T., 2025. Coupled ground subsidence and rapid urbanization of the Red River delta region and the city of Hanoi, Vietnam, revealed through a Multi-Track InSAR analysis. International Journal of Applied Earth Observation and Geoinformation, 144, 104886. https://doi.org/10.1016/j.jag.2025.104886.

Zhao R., Arabameri A., Santosh M., 2024. Land subsidence susceptibility mapping: a new approach to improve decision stump classification (DSC) performance and combine it with four machine learning algorithms. Environmental Science and Pollution Research, 31(10), 15443−15466. https://doi.org/10.1007/s11356-024-32075-w.

APPENDIX

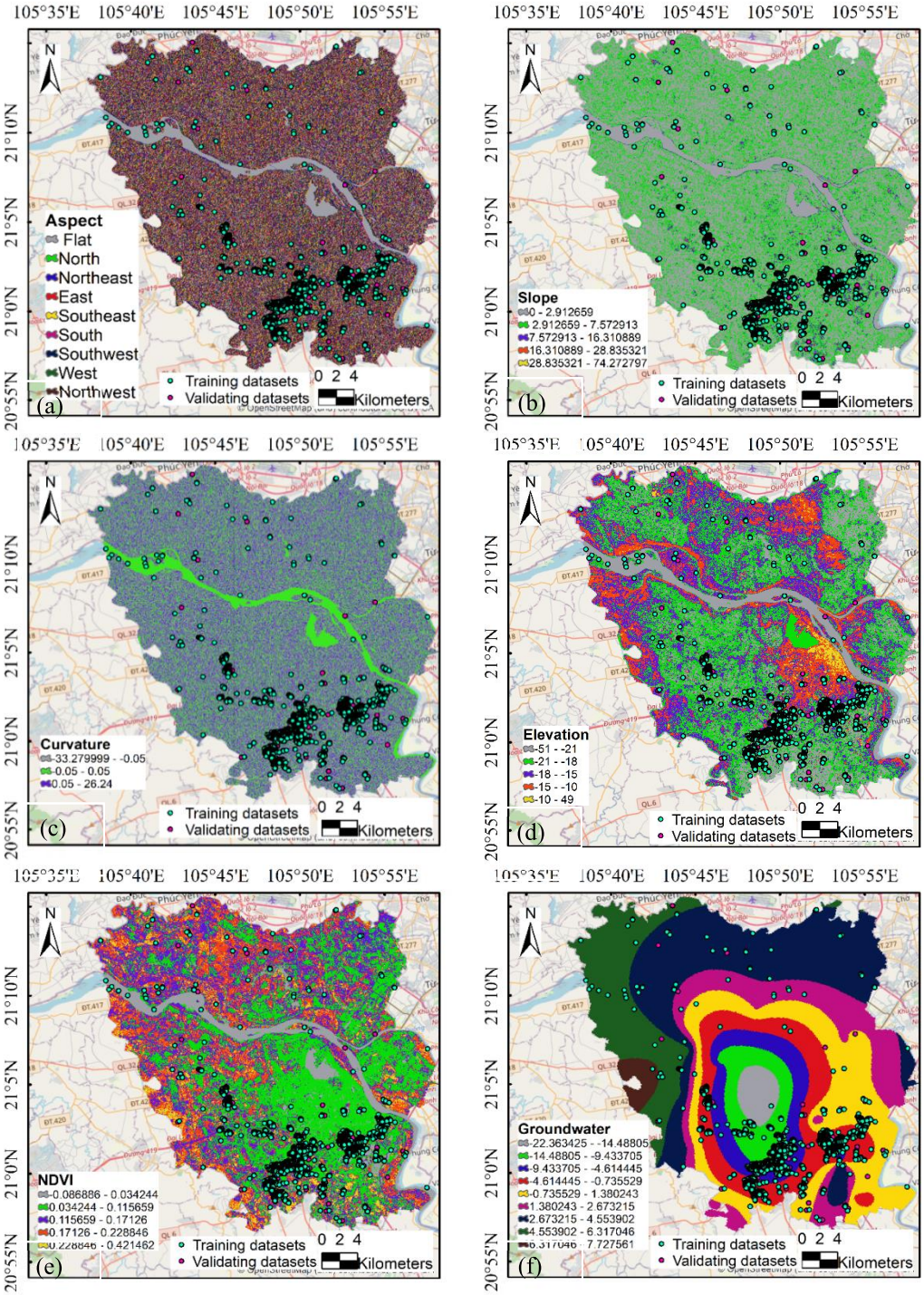

Appendix A. Thematic maps of the study area: (a) Aspect; (b) Slope; (c) Curvature; (d) Elevation; (e) NDVI; (f) Groundwater

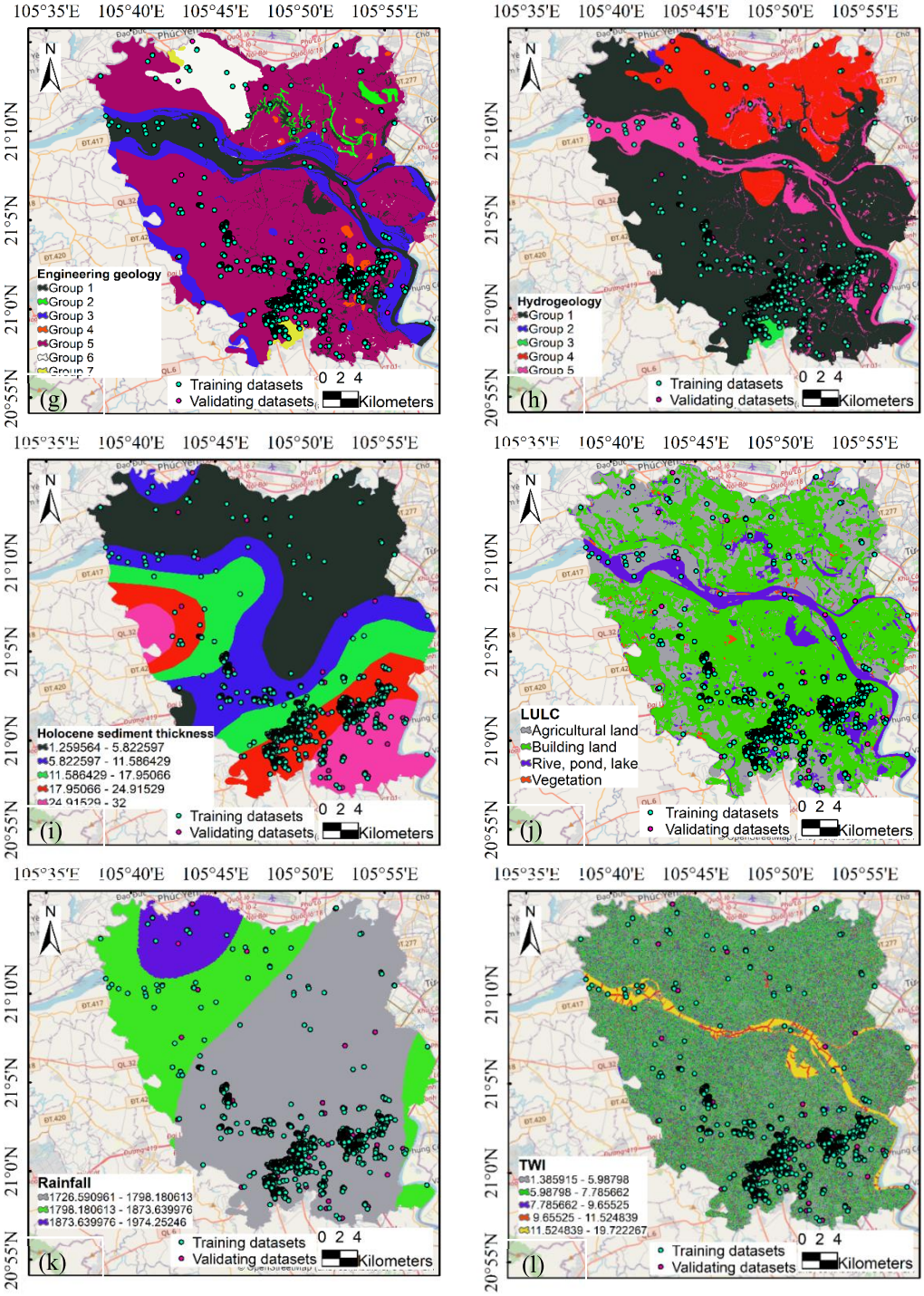

Appendix A. Cont. (g) Engineering geology; (h) Hydrogeology; (i) Holocene sediment thickness; (j) LULC; (k) Rainfall; (l) TWI

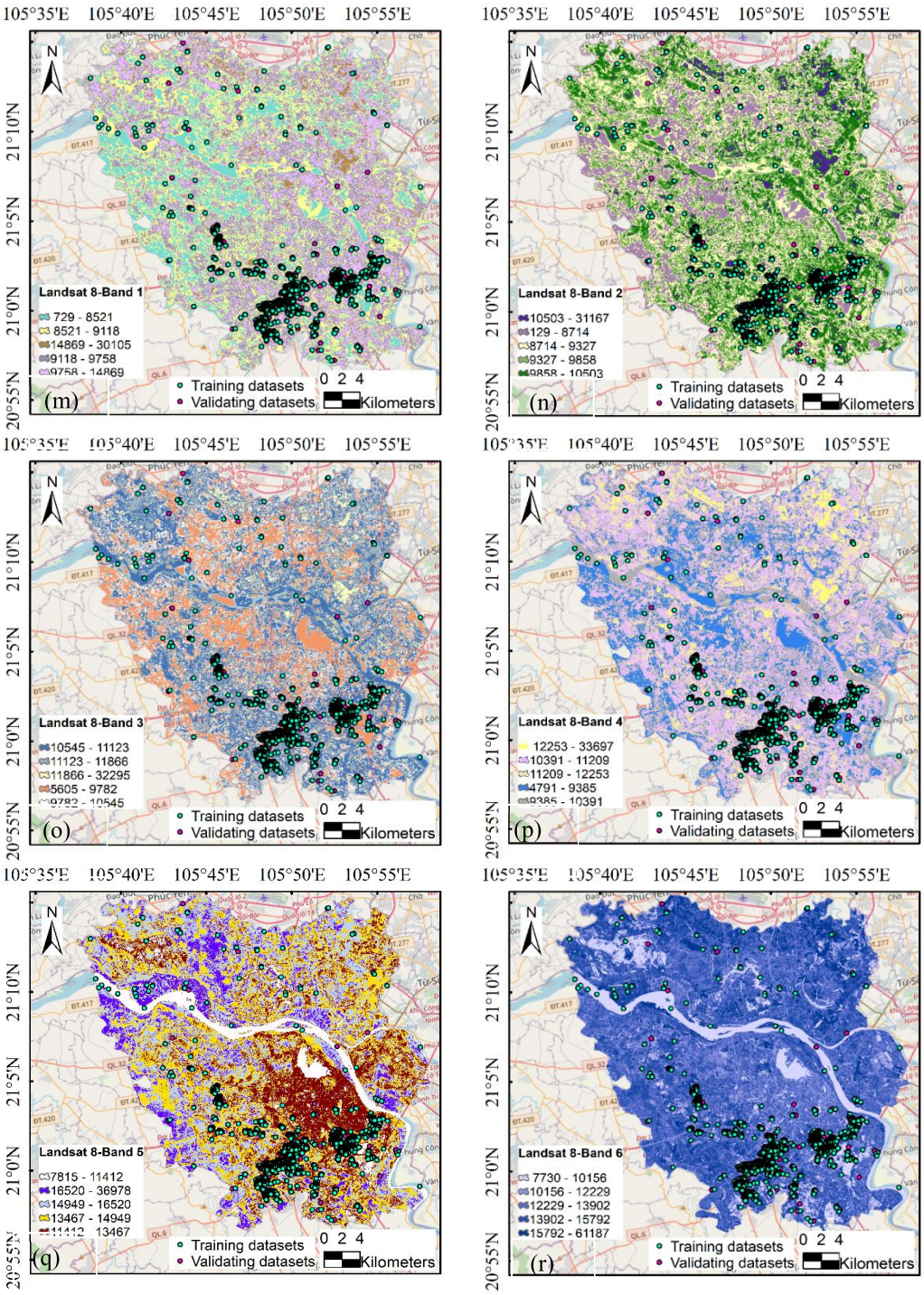

Appendix A. Cont. (m) Landsat 8-Band 1; (n) Landsat 8-Band 2; (o) Landsat 8-Band 3; (p) Landsat 8-Band 4; (q) Landsat 8-Band 5; (r) Landsat 8-Band 6

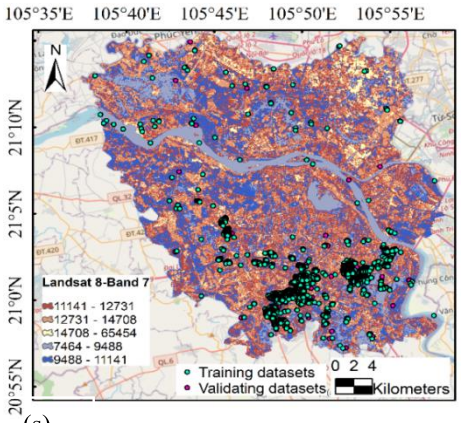

Appendix A. Cont. (s) Landsat 8-Band 7

Appendix B. Hyperparameters of the developed deep learning models

Hyperparameters	CNN	LSTM	DRDN	CNN–LSTM
Kernel size	3	—	—	3
LSTM units	—	32	—	128
Block units	—	—	128	—
Number of blocks	—	—	8	—
Dense units	128, 64	—	64, 32	64
Dropout	0.3	—	0.2, 0.3	0.2
Optimizer	SGD	Adam	Adam	Adam
Learning rate	—	—	1.00E-03	0.05
Batch size	32	32	32	32
Epochs	1000	1000	1000	1000

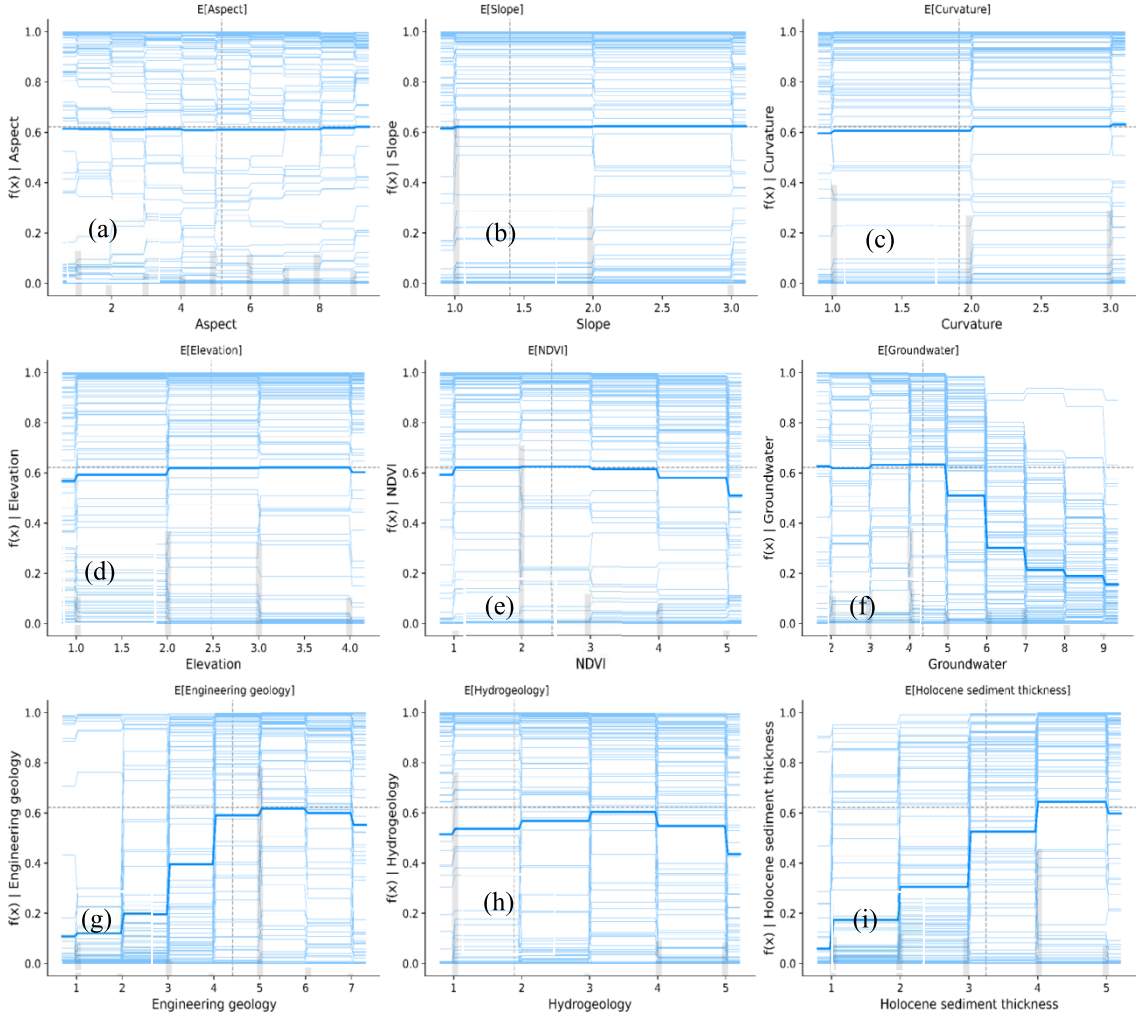

Appendix C. Cont. SHAP dependence (ICE) plots illustrating the effects of conditioning factors on land subsidence prediction: (a) Aspect; (b) Slope; (c) Curvature; (d) Elevation; (e) NDVI; (f) Groundwater; (g) Engineering geology; (h) Hydrogeology; (i) Holocene sediment thickness

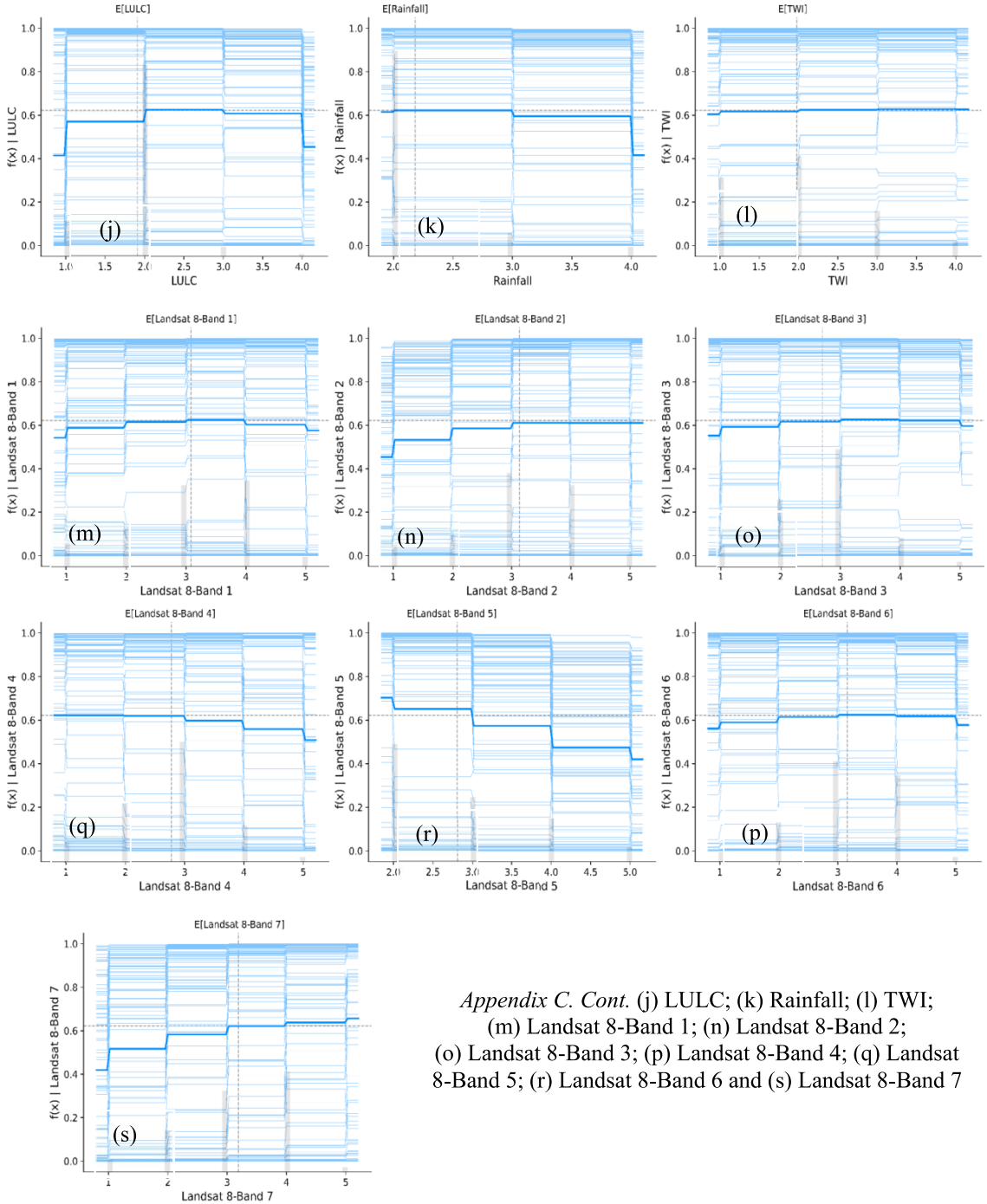

Appendix C. Cont. (j) LULC; (k) Rainfall; (l) TWI; (m) Landsat 8-Band 1; (n) Landsat 8-Band 2; (o) Landsat 8-Band 3; (p) Landsat 8-Band 4; (q) Landsat 8-Band 5; (r) Landsat 8-Band 6 and (s) Landsat 8-Band 7